Real-time Improved Nearest Level Control for Power Electronics Building Blocks in All-Electric Ship Power Systems

Ali Moghassemi, *Graduate Student Member, IEEE*, Laxman Timilsina, *Member, IEEE*, S M Imrat Rahman, *Graduate Student Member, IEEE*, Ali Arsalan, *Graduate Student Member, IEEE*, Grace Muriithi, *Graduate Student Member, IEEE*, Elutunji Buraimoh, *Member, IEEE*, Gokhan Ozkan, *Senior Member, IEEE*, Behnaz Papari, *Senior Member, IEEE*, Christopher S. Edrington, *Senior Member, IEEE*, Zheyu Zhang, *Senior Member, IEEE*, and Phani Kumar Chamarthi, *Member, IEEE*

***Abstract*—Power electronics building block (PEBB) concept involves integrating fundamental components into functional blocks that can be stacked, extending converter power ratings for all-electric ships (AESs). This modular approach reduces costs, size, weight, design complexity, and maintenance. PEBBs can be realized as modular multi-level converters (MMCs), which offer advantages like modularity, low switching losses, minimal voltage/current quantization, high reliability, and efficiency. However, effective switching control methods are crucial to balance capacitor voltages and suppress circulating currents. This paper proposes an improved nearest level control (NLC) method that employs smoothed trapezoidal reference signals instead of sinusoidal references, aiming to enhance capacitor voltage balancing, suppress circulating currents, and improve the output power quality of PEBBs in AESs. The proposed NLC method is analyzed in real-time for an N-level PEBB connected to an induction machine (IM) with variable speed and torque load. The real-time verification is conducted in the Typhoon HIL606 digital real-time simulator (DRTS). The results validate the feasibility and effectiveness of the proposed NLC method for a three-phase N-level PEBB concept for AESs.**

***Index Terms*—Power electronics building block (PEBB), modular multi-level converter (MMC), nearest level control (NLC), capacitor voltage balancing, circulating current suppression.**

Received 27 September 2024; revised 14 January 2025; accepted 24 March 2025. Date of publication 9 April 2025; date of current version 20 September 2025. Paper 2024-TSC-1406.R1, presented at the 2024 IEEE Transportation Electrification Conference and Expo, Chicago, IL, USA, Jun. 19–21, and approved for publication in the IEEE TRANSACTIONS ON INDUSTRY APPLICATIONS by the Transportation Systems Committee of the IEEE Industry Applications Society [DOI: 10.1109/ITEC60657.2024.10598932]. This work was supported by the US Office of Naval Research (ONR) under Award N00014-22-1-2558 and was authorized for public release under Grant DCN 0543-1443-24. *(Corresponding author: Ali Moghassemi.)*

Ali Moghassemi, Laxman Timilsina, S M Imrat Rahman, Elutunji Buraimoh, and Christopher S. Edrington are with the Real-Time COntrol and Optimization Laboratory (RT-COOL), Holcombe Department of Electrical and Computer Engineering, Clemson University, Clemson, SC 29634 USA (e-mail: amoghas@clemson.edu; ltimils@clemson.edu; smimrar@clemson.edu; eburaim@clemson.edu; cedring@clemson.edu).

Ali Arsalan and Grace Muriithi are with the Department of Automotive Engineering, Clemson University, Greenville, SC 29607 USA (e-mail: aarsala@clemson.edu; gmuriit@clemson.edu).

Gokhan Ozkan is with the Real-Time COntrol and Optimization Laboratory (RT-COOL), Holcombe Department of Electrical and Computer Engineering, Clemson University, Clemson, SC 29634 USA, and also with the Dominion Energy Innovation Center, Clemson University, North Charleston, SC 29405 USA (e-mail: gokhano@clemson.edu).

Behnaz Papari is with the Real-Time COntrol and Optimization Laboratory (RT-COOL), Holcombe Department of Electrical and Computer Engineering, Clemson University, Clemson, SC 29634 USA, and also with the Department of Automotive Engineering, Clemson University, Greenville, SC 29607 USA (e-mail: bpapari@clemson.edu).

Zheyu Zhang is with the Electrical, Computer, and Systems Engineering, Rensselaer Polytechnic Institute, Troy, NY 12180 USA (e-mail: zhangz49@rpi.edu).

Phani Kumar Chamarthi is with the Environmental Research and Innovation Department, Luxembourg Inst. Science & Technology (ICES), 4362 Belval, Luxembourg (e-mail: phanikumaree@gmail.com).

Color versions of one or more figures in this article are available at https://doi.org/10.1109/TIA.2025.3559049.

Digital Object Identifier 10.1109/TIA.2025.3559049

NOMENCLATURE

Abbreviations

AES	All-Electric Ship.
$DRTS$	Digital Real-Time Simulator.
$IFOC$	Indirect Field-Oriented Control.
$IGBT$	Insulated Gate Bipolar Transistor.
IM	Induction Machine.
$LOESS$	Locally Estimated Scatterplot Smoothing.
LRU	Least Replacement Unit.
MLC	Multilevel Converter.
MMC	Modular Multilevel Converter.
ONR	Office of Naval Research.
$PEBB$	Power Electronics Building Block.
PWM	Pulse Width Modulation.
QOS	Quality Of Service.
SM	Submodule.
THD	Total Harmonic Distortion.

Parameters and Variable

$\lambda_{abcs}, \lambda_{abcr}$	Stator and rotor flux linkages.
$\overline{V_{C,aU}}, \overline{V_{C,aL}}$	Mean capacitor voltage of upper/lower arms.
i_{abcs}, i_{abcr}	Stator and rotor currents.
i_{aL}, i_{bL}, i_{cL}	Lower arm currents of all phases.
i_{aU}, i_{bU}, i_{cU}	Upper arm currents of all phases.

i_a, i_b, i_c	Output currents of all phases.
$i_{c_a}, i_{c_b}, i_{c_c}$	Circulating currents of all phases.
i_{CU}, i_{CL}	Capacitor current of upper/lower arms.
L_{arm}, R_{arm}	Arm inductor and resistor.
L_{lr}, L_{mr}	Rotor's leakage/magnetizing inductances.
L_{ls}, L_{ms}	Stator's leakage/magnetizing inductances.
L_M	Mutual inductance.
N, n	Number of voltage levels, and SMs per arm.
$n_{SM,L}, n_{SM,U}$	Connected SMs of the lower/upper arms.
r_s, r_r	Stator and rotor resistances.
$V^1_{C,aU}$ to $V^n_{C,cL}$	SM Capacitor voltages.
$V^{ref}_{aU}, V^{ref}_{aL}$	Normalized reference voltage.
V^{ref}_{PEBB}	Nearest integer value for the PEBB.
V^*_C	Nominal capacitor voltage.
V_{abcs}, V_{abcr}	Stator and rotor voltages.
V_{ab}, V_{bc}, V_{cs}	Line-to-line voltages.
V_{aL} to V_{cL}	Lower arm voltages of all phases.
V_{aU} to V_{cU}	Upper arm voltages of all phases.
V_a, V_b, V_c	Line-to-neutral voltages.
V_{CU}, V_{CL}	Capacitor voltage of upper/lower arms.
V_{dc}	DC-link voltage.

I. Introduction

A. Literature Review

THE rising power demand in modern naval ships has spurred the development of all-electric ships (AESs) that utilize electrical energy for propulsion, weapons, and supply services. These ship systems employ power electronic interfaces to connect loads to their energy source, fueling interest in multi-functional power converters for energy conversion and management [1]. Emerging technologies like wide bandgap materials, silicon carbide power semiconductors, and power electronics building blocks (PEBB) are transforming marine systems, departing from traditional steamships and sailing vessels. Advances in the PEBB, stemming from a 1998 proposal by the US Office of Naval Research (ONR) to enhance converter availability, performance, and cost-effectiveness, have had a profound impact on converter innovation, manufacturing, commissioning, and operation in electric ship applications [2].

A metric for assessing the quality of service (QOS) is crucial in the shipboard power systems' planning, certification, and operation [3]. This metric revolves around the likelihood of the power system delivering the necessary continuity to support various loads essential for the ship's missions. Key determinants affecting QOS include prime movers' ratings, reliability and failure patterns, power conversion gear, load equipment, and overall system setup. Where feasible, power conversion devices should integrate features like hot-swappable power modules and ample redundancy and capacity to facilitate module replacement without compromising QOS, a principle known as the least replacement unit (LRU). Consequently, AESs demand power electronics equipment that maintains a compact ship size and concurrently enhances availability and reliability. This involves ensuring high-quality power distribution to propulsion motors while addressing mechanical flaws and modifications. From a control viewpoint, challenges in power converters of AESs largely stem from power quality, thermal stress, and voltage stresses on semiconductors [4].

The shipboards use multiple power converters, advancing topology, voltage stability analysis, power quality, fault detection, and protection. Innovative multi-level converter (MLC) topologies, introduced in [5], enhance power ratings, cost-effectiveness, availability, and overall performance in AESs. MLCs produce AC voltages using multiple DC voltage levels, yielding benefits like reduced AC ripple, lower stress on power semiconductors and loads, and a higher switching frequency. Diverse MLC types, such as neutral-point clamped converters, flying capacitor converters, cascaded H-bridge converters, and modular multi-level converters (MMC), are recent developments [6]. A comprehensive review in [7] explored MLC applications in various fields, revealing their benefits, such as lower total harmonic distortion (THD), reduced input current distortion, and decreased switching frequency for lower switching losses. Yet, more components can lead to lower reliability, increased costs, and complex controllers.

The MMC configuration, a recent advancement in MLC technology, consolidates the benefits of MLC topologies sans the necessity for isolated DC sources and intricate phase-shifting transformers. Operating across voltage levels ranging from medium (2.3-13.8 kV) to high-voltage (33-400 kV), MMCs support power ratings spanning from 226 kW to 1000 MW [8]. This versatility renders MMCs applicable across diverse transportation sectors, including electric railway traction [9], railway power supplies [10], energy storage systems [11], batteries [12], electric vehicles [13], and notably, naval electric ship systems [14]. MMC topology offers structural modularity, simplicity, scalability, robust fault ride-through capability, minimal voltage/current quantization, minimal filter requirements, low switching frequency, submodule (SM) bypassing without converter tripping, high reliability, and efficiency [5]. Recent developments based on MMC configuration aim to refine the PEBB concept for enhancing shipboard electric power systems, focusing on improving reliability, modularity, scalability, and fault-ride-through capability while reducing production and maintenance costs and minimizing voltage and current quantization [15].

In fundamental switching frequency modulation, the NLC method, known for its carrier-less approach, has gained popularity over carrier-based ones for its flexibility and simplicity [16]. NLC derives switching configurations and durations directly from the desired voltage without carrier signals. Traditional NLC works best in MMCs with a reasonably high number of SMs per arm (e.g. 80 SMs in [17], 20 SMs in [18]) to maintain an acceptable voltage quality [19], which may reduce the voltage quality of MMCs with only a few SMs. In one approach [20], NLC is combined with carrier-based pulse width modulation (PWM) to enhance output quality, though at the expense of increased switching losses compared to traditional NLC. Another technique [21] introduces a new NLC method to enhance MMC output as the number of levels increases, validated via simulations and comparisons with traditional NLC in MMCs with 18 SMs. An alternative NLC variation [22] aims to increase voltage levels using sinusoidal signal references and a modified rounding function, validated through simulations and experiments with 10 SMs. Ref. [23] addresses THD reduction through third-harmonic injection-based schemes, comparing them with traditional NLC, with good outcomes depicted using 30 SMs. Ref. [16] presents an improved NLC method that uses first-order two-variable relations to suppress circulating current, which is particularly beneficial for MMCs with 7 SMs. The method's effectiveness is validated through simulations and experiments in a single-phase MMC system. Also, [24] introduces an enhanced NLC technique involving slight offset addition and alternating at twice the fundamental frequency in reference signals, with performance verification conducted through simulations and experiments using 8 SMs.

The aforementioned NLC methods can raise several challenges, such as poor output voltage and current quality, high THD, high SM capacitor voltage ripples, unsuppressed circulating currents, and computational burden. These issues become more pronounced as the number of SMs increases, such as the PEBBs concept used in AESs. To ensure optimal performance, the NLC method must simultaneously maintain effective control of capacitor voltage balancing, suppress circulating current, mitigate arm voltage stresses, meet the power quality requirements, and reduce complexity.

B. Contribution of the Paper

This study endeavors to enhance the performance of PEBB in AESs via the proposed NLC method. Implementing an improved switching method can further elevate PEBB's power quality while controlling the SM capacitor voltages and circulating currents. The proposed method is a significant extension of our previous work [25] where the NLC method was introduced using sinusoidal references, and only a 5-level PEBB connected to a resistive-inductive RL load was analyzed in MATLAB/Simulink. The main contributions of this paper are as follows:

- Introduction of an improved and adaptable N-level NLC switching method tailored for N-level PEBBs in AESs, offering flexibility to adjust voltage levels as required while reducing the complexity by using smoothed trapezoidal voltage references rather than sinusoidal ones.
- Enhancement of PEBB's performance through simultaneous improvement of power quality, capacitor voltage balancing, and circulating current suppression.
- Real-time validation on an IM, representative of AES conditions, featuring variable speed and torque loads controlled through a closed-loop indirect field-oriented control (IFOC) method.
- Evaluation of the performance of the proposed NLC method across varying load conditions, including variable speed and torque loads, highlighting its real-time feasibility.
- Real-time validation of the proposed NLC method using the Typhoon HIL606 DRTS, affirming its effectiveness in practical applications.

The paper is structured as follows. Section II introduces the PEBB concept and its mathematical model. Section III presents the traditional and the proposed NLC method with smoothed trapezoidal reference signals, along with its impact on enhancing the performance of the PEBB connected to an IM. Section IV presents the mathematical model of the IM, including voltage and torque equations in machine variables. Section V presents real-time simulation results of 9 L/7L/5 L PEBBs using the proposed NLC method under various speed and torque load conditions, as well as THD analyses and comparisons. Finally, Section VI concludes the paper.

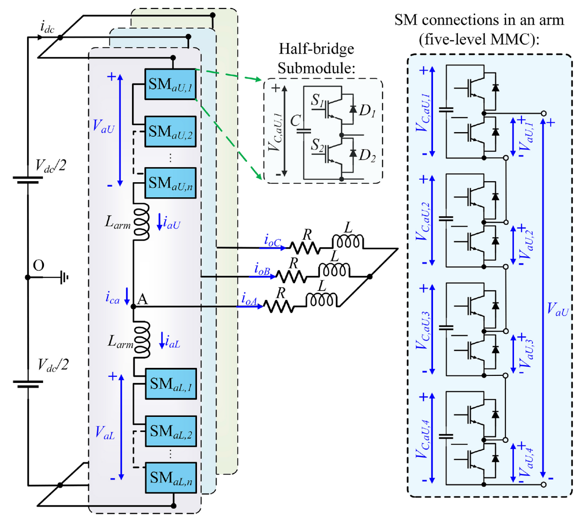

Fig. 1. Three-phase MMC configuration and SM connection [25].

II. Modular Multi-Level Converter (MMC)

A. Principal

Fig. 1 illustrates the three-phase MMC configuration, consisting of three legs corresponding to the three phases. Each leg comprises two arms (upper and lower), with each arm housing n identical half-bridge SMs connected in series. These SMs can be full-bridge, half-bridge, or a combination. In this paper, the half-bridge SM configuration is used, which includes two complementary IGBTs with anti-parallel diodes and a parallel capacitor. Additionally, each leg includes an inductor (L_{arm}) to limit short-circuit currents and may incorporate a series resistor (R_{arm}) to reduce MMC's power losses.

It bears noting that the equations are presented for phase a, and similar steps can be applied to the phases. In Fig. 1, the output terminals of the SMs are connected in series to form an arm voltage (V_{aU} in this case), with $V_{aU,1}$, $V_{aU,2}$, $V_{aU,3}$, and $V_{aU,4}$ representing the output voltages of the SMs. V_{aU} denotes the arm voltage. In this study, subscripts a, b, and c indicate the three phases, U and L denote the upper and lower arms, and $n = 1, 2, 3, \ldots, n$ signifies the number of SMs. In Fig. 1, L_{arm} represents the arm inductance; V_{aU}, V_{bU}, and V_{cU} are the upper arm voltages; V_{aL}, V_{bL}, and V_{cL} are the lower arm voltages; i_{aU}, i_{bU}, and i_{cU} denote the upper arm currents; i_{aL}, i_{bL}, and i_{cL} represent the lower arm currents; i_{OA}, i_{OB}, and i_{OC} are the output currents; i_{c_a}, i_{c_b}, and i_{c_c} signify the circulating currents; V_{dc} represents the DC source voltage, and $V_{C,aU,1}$ to $V_{C,cL,n}$ are the SM capacitor voltages. The number of SMs in

TABLE I
SWITCHING STATES OF AN SM (E.G., $SM_{aU,1}$) [25]

S_1	S_2	D_1	D_2	i_{arm}	Capacitor State	$V_{aU,1}$
0	1	0	0	>0	Unchanged	0
0	0	0	1	<0	Unchanged	0
0	0	1	0	>0	Charging	V_c
1	0	0	0	<0	Discharging	V_c

the arm determines the converter output level. With n SMs in each arm, the line-to-neutral and line-to-line voltages have $n+1$ and $2n+1$ levels, respectively, based on the state of each SM, which can be connected or bypassed. Note that the IGBTs in each SM are complementary. When one IGBT is ON, the other is OFF, and vice versa. Thus, an SM is connected when the upper IGBT is ON and bypassed when the upper IGBT is OFF. Table I presents the switching states of the SM.

B. Mathematical Model

Applying Kirchhoff's current law (KCL) in Fig. 1, the output current can be expressed as:

$$i_{OA} = i_{aU} - i_{aL} \tag{1}$$

The circulating current is obtained as the mean value of the upper and lower arm currents, expressed as:

$$i_{c_a} = (i_{aU} + i_{aL})/2 \tag{2}$$

Applying Kirchhoff's voltage law (KVL), the upper and lower voltage legs are expressed in (3) and (4), respectively:

$$\frac{V_{dc}}{2} - V_{aU} - L_{arm}\frac{di_{aU}(t)}{dt} - Ri_{OA} - L\frac{di_{OA}(t)}{dt} = 0 \tag{3}$$

$$-\frac{V_{dc}}{2} + V_{aL} + L_{arm}\frac{di_{aL}(t)}{dt} - Ri_{OA} - L\frac{di_{OA}(t)}{dt} = 0 \tag{4}$$

Using i_{OA} from (1) and adding it to the sum of (3) and (4), the output voltage of phase a (V_{OA}) is expresses as follows:

$$V_{OA} = Ri_{OA} + L\frac{di_{OA}(t)}{dt} = \frac{V_{aL} - V_{aU}}{2} - \frac{L_{arm}}{2}\frac{di_{OA}(t)}{dt} \tag{5}$$

The upper and lower arm voltages of phase a can also be expressed as follows:

$$V_{aU} = n_{SM,U}\overline{V_{C,aU}} \tag{6}$$

$$V_{aL} = n_{SM,L}\overline{V_{C,aL}} \tag{7}$$

In (6) and (7), $n_{SM,U}$ and $n_{SM,L}$ represent the number of connected SMs in the upper and lower arms of phase a, respectively. $\overline{V_{C,aU}}$ and $\overline{V_{C,aU}}$ denote the mean values of the capacitor voltages in the upper and lower arms of phase a, respectively. Assuming the SM capacitor voltages remain constant at their nominal levels ($V_C^* = V_{dc}/(N-1)$) and the voltage drop across the arm inductors is negligible, the output voltage of phase a can be expressed as follows:

$$V_{OA} = ((n_{SM,L} - n_{SM,U})/2)V_C^* \tag{8}$$

Fig. 2 depicts an MMC implementation using a switching function, representing the equivalent circuit of the MMC leg.

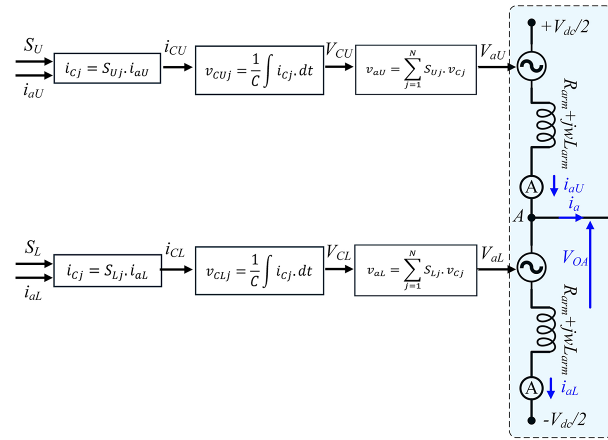

Fig. 2. Equivalent circuit of an MMC leg.

III. PROPOSED NEAREST LEVEL CONTROL (NLC) METHOD

For proper MMC operation, it's essential to maintain the average voltage stress across each SM capacitor at $V_{dc}/(N-1)$. Here, V_{dc} stands for the DC-link voltage, and $N = n+1$ is the number of levels. The output phase voltage V_{OA} can be represented by using either the upper or lower arm SM capacitor voltage, as follows:

$$V_{aU} = \frac{V_{dc}}{2} - \sum_{j=1}^{n} S_{Uj}V_{CUj} - L_{arm}\frac{di_{aU}(t)}{dt} \tag{9}$$

$$V_{aL} = -\frac{V_{dc}}{2} + \sum_{j=1}^{n} S_{Lj}V_{CLj} + L_{arm}\frac{di_{aL}(t)}{dt} \tag{10}$$

The voltage across any selected SM capacitor in phase a, whether from the upper or lower arms, can be described with either of the below equations as follows:

$$V_{CUj} = \frac{1}{C}\int S_{Uj}i_{aU}(t)\,dt \tag{11}$$

$$V_{CLj} = \frac{1}{C}\int S_{Lj}i_{aL}(t)\,dt \tag{12}$$

As shown in Fig. 2, the arm current (i_{aU} for the upper arm or i_{aL} for the lower arm) is taken and based on the switching pulses (S_U for the upper arm or S_L for the lower arm) created by the proposed NLC, the capacitor current (i_{CU} for the upper arm or i_{CL} for the lower arm) is calculated. Then, based on this current, the capacitor voltage (V_{CU} for the upper arm or V_{CL} for the lower arm) is calculated, which will be used for calculating the arm voltage (V_{aU} for the upper arm or V_{aL} for the lower arm).

As an example, in the case of a five-level MMC ($n=4$), the arm voltage ranges from 0 to $4V_C$, with $4V_C$ representing the highest level (achieved by turning ON all switches) and 0 the lowest level (achieved by turning OFF all switches). The intermediate levels are generated through various switching combinations, known as redundancy switching states, designed to balance the capacitor voltages of the SMs. Fig. 3 shows phase unit stages and voltages of the single-phase 5L MMC

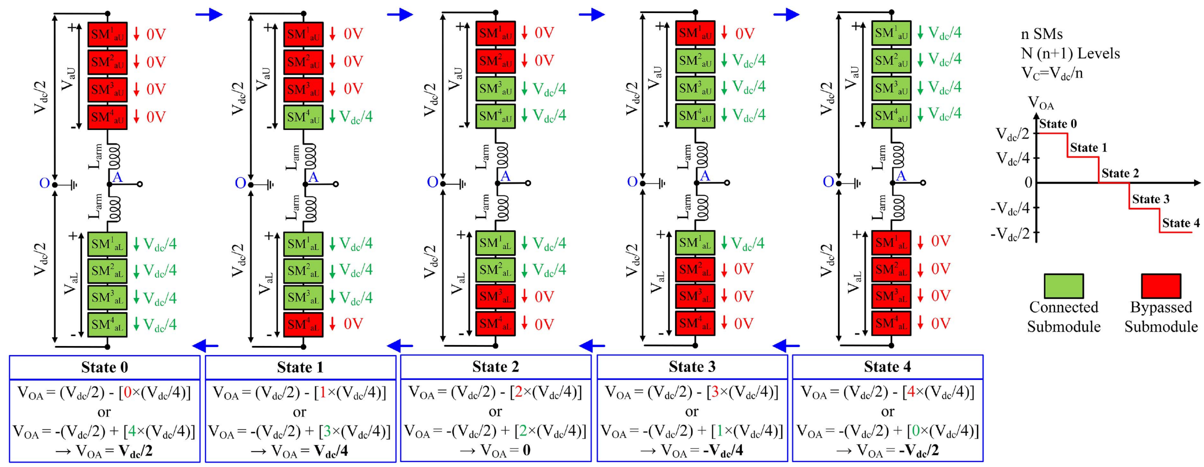

Fig. 3. Phase unit stages and voltages of a single-phase 5 L PEBB [25].

TABLE II
SWITCHING STATES AND VOLTAGE LEVELS OF A 5 L MMC [25]

S_1	S_2	S_3	S_4	$V_{aU,1}$	$V_{aU,2}$	$V_{aU,3}$	$V_{aU,4}$	V_{aU}	Level
0	0	0	0	0	0	0	0	0	0
1	0	0	0	V_C	0	0	0	V_C	1
0	1	0	0	0	V_C	0	0	V_C	
0	0	1	0	0	0	V_C	0	V_C	
0	0	0	1	0	0	0	V_C	V_C	
1	1	0	0	V_C	V_C	0	0	$2V_C$	2
1	0	1	0	V_C	0	V_C	0	$2V_C$	
1	0	0	1	V_C	0	0	V_C	$2V_C$	
0	1	1	0	0	V_C	V_C	0	$2V_C$	
0	1	0	1	0	V_C	0	V_C	$2V_C$	
0	0	1	1	0	0	V_C	V_C	$2V_C$	
1	1	1	0	V_C	V_C	V_C	0	$3V_C$	3
1	1	0	1	V_C	V_C	0	V_C	$3V_C$	
1	0	1	1	V_C	0	V_C	V_C	$3V_C$	
0	1	1	1	0	V_C	V_C	V_C	$3V_C$	
1	1	1	1	V_C	V_C	V_C	V_C	$4V_C$	4

configuration. For instance, the switching states, SM output voltages, and arm voltages are presented in Table II in which the arm voltage can be expressed as follows:

$$V_{aU} = \sum_{i=1}^{n} V_{aU,i} = \sum_{i=1}^{n} S_i V_C \tag{13}$$

Switching control methods for MMC can be categorized based on the switching frequency range. Low-frequency switching control methods benefit high-level MMC applications (e.g., PEBBs in AESs). They allow the effortless generation of staircase-like output voltage, reducing voltage and current quantization. Consequently, this leads to lower filter requirements (often no filter) and decreased power losses. Note that the NLC method is more suitable for high-level MMC applications with many SMs, as it may compromise voltage quality when applied to low SM configurations.

The output voltage in Fig. 2 can be also expressed as:

$$V_a = M\frac{V_{dc}}{2}\sin(\omega t + \theta) \tag{14}$$

Where M, ω, and θ represent the modulation index, fundamental angular frequency, and phase angle, respectively. Thus, the upper/lower arm voltages can be re-written as follows:

$$V_{aU} = \frac{V_{dc}}{2} - M\frac{V_{dc}}{2}\sin(\omega t + \theta) \tag{15}$$

$$V_{aL} = -\frac{V_{dc}}{2} + M\frac{V_{dc}}{2}\sin(\omega t + \theta) \tag{16}$$

Considering $V_C = V_{dc}/n$ or $V_C = V_{dc}/(N-1)$), the above equations can be re-written as follows:

$$V_{aU} = \left(\frac{nV_C}{2}\right) - M\left(\frac{nV_C}{2}\right)\sin\left(\omega t + \theta\right) \tag{17}$$

$$V_{aL} = -\left(\frac{nV_C}{2}\right) + M\left(\frac{nV_C}{2}\right)\sin\left(\omega t + \theta\right) \tag{18}$$

The NLC method, known as the round method, selects the nearest voltage level produced during the conversion process to match the desired output voltage reference. This approach enables independent control of the three phases through separate comparisons. Fig. 4(a) shows a single-phase MMC (5 L, 7 L, and 9 L) phase unit's stages and voltages. Fig. 4(b) shows how the reference value is compared with the current voltage level to create a staircase pattern. The NLC output voltage is determined by comparing the reference voltage with the current output voltage. To specify the number of SMs required to reach the next voltage level, the round function is used, which rounds the input signal to the nearest value. These reference values are initially normalized. The normalized reference voltage can be expressed as follows:

$$V_{aU}^{ref} = \left(\frac{n}{2}\right)\left(1 - M\sin\left(\omega t + \theta\right)\right) \tag{19}$$

$$V_{aL}^{ref} = \left(\frac{n}{2}\right)\left(1 + M\sin\left(\omega t + \theta\right)\right) \tag{20}$$

To create V_{aU}^{ref} or V_{aL}^{ref}, the error between the IM speed and speed desired by the user is taken and three reference voltages are then created as per the desired speed. These are a function of $V_{pu}\sin(\omega t + \theta)$, where V_{pu} can act as the modulation index ranging within $0 < V_{pu} < 1$, ω and θ denote angular frequency and phase angle, respectively. Then, these normalized reference

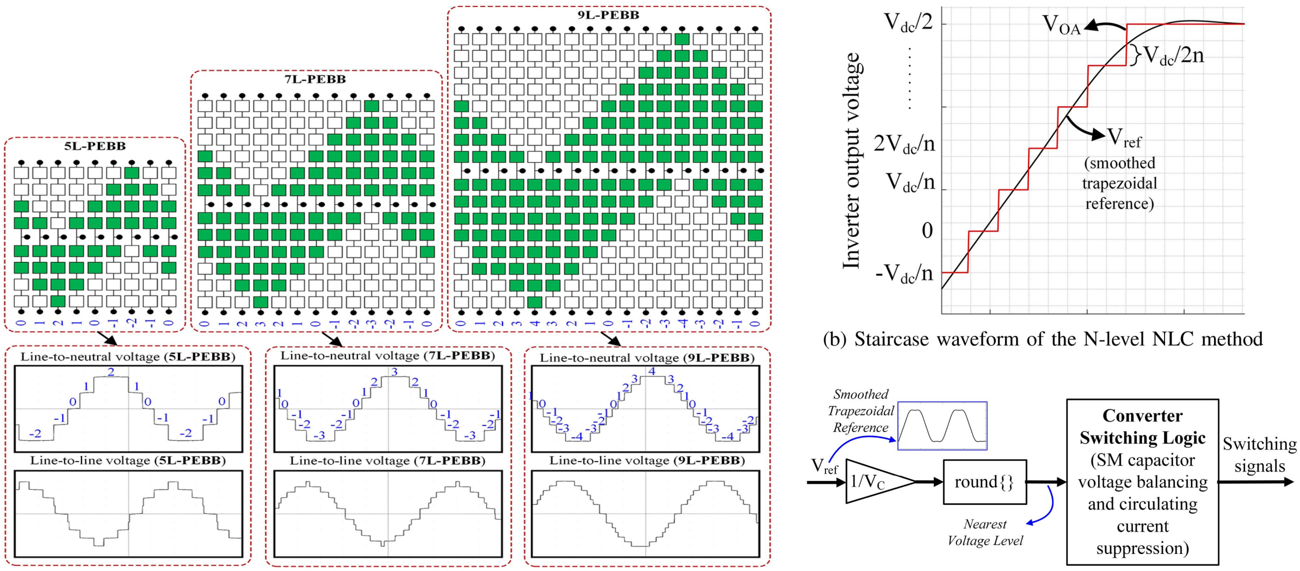

(a) Phase unit stages to shape staircase waveforms of the PEBB (phase a)

(b) Staircase waveform of the N-level NLC method

(c) Producing switching pulses with the round function

Fig. 4. Working principle of the proposed NLC method with smoothed trapezoidal reference signals.

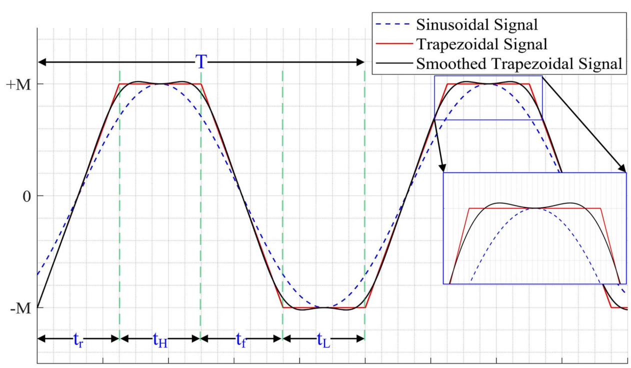

Fig. 5. Sinusoidal [25], traditional [27], and the proposed smoothed trapezoidal signals.

voltages undergo rounding to find the nearest integer value for the MMC topology:

$$V_{PEBB_U}^{ref} = round(V_{aU}^{ref}) \quad (21)$$

$$V_{PEBB_L}^{ref} = round(V_{aL}^{ref}) \quad (22)$$

The round function provides the closest integer of the input value (e.g., round(1.4)=1, or round(−2.9)=−3). Fig. 4(c) illustrates the principle of the NLC method for producing switching pulses considering SM capacitor balancing and circulating current suppression. In this paper, an improved trapezoidal signal is used instead of the sinusoidal signal as a reference waveform to obtain improved output quality and control the modulation process. A trapezoidal waveform can be realized as an intermediate waveform between a square-wave signal and a triangular signal [26]. As can be seen in Fig. 5, it is composed of four segments: the rise time (t_r), high time (t_H), fall time (t_f), and low time (t_L). For an alternating trapezoidal signal with a normalized amplitude of M, the voltage varies linearly from the minimum value ($-M$) to the maximum value ($+M$) during the rise time (t_r). During t_H, the signal is held to the highest value ($+M$). During t_f, the signal changes linearly from the highest value ($+M$) to the lowest value ($-M$). During t_L, the signal is held to the lowest value ($-M$). A complete period of the trapezoidal signal consists of these four segments, as follows [26]:

$$T = t_r + t_H + t_f + t_L \quad (23)$$

It bears noting that the trapezoidal signal is symmetry if $t_r = t_f$ and $t_H = t_L$. The signal is a square wave with a 0.5 duty cycle if $t_r = t_f = 0$. In other words, $t_H = t_L = T/2$. Similarly, it is a triangular waveform if $t_r = t_f = T/2$. In other words, $t_H = t_L = 0$. Thus, equation (14) can now modified by using a trapezoidal waveform (tr), as follows [27]:

$$V_a = M\frac{V_{dc}}{2}tr(\omega t + \theta) \quad (24)$$

This signal uses linear segments for the rise and fall times, which leads to abrupt transitions between different regions (rise, flat, fall). These sharp transitions generate higher-order harmonics, which can degrade the output waveform quality. In this paper, the trapezoidal waveform is improved by smoothing out the transitions between the flat and sloped regions of the trapezoidal signal to reduce the generation of higher-order harmonics. To this end, some smoothing techniques exist, such as spline interpolation or a low-pass filter. The goal is to generate a more gradual change in the signal, which helps in reducing high-frequency harmonics. Sharp changes in a waveform contribute to a wide range of higher-order harmonics. Smoothing these changes lowers the harmonic content, which is desirable in motor drive systems, particularly this paper's application, the PEBBs concept for AESs. In this paper, the Locally Estimated Scatterplot Smoothing (LOESS) was applied. LOESS smoothing is a local regression method that fits smooth curves to sections of the data. It works by performing a weighted least squares regression in localized neighborhoods of the signal. If the traditional trapezoidal waveform can be formed by (25):

$$tr(t) = \begin{cases} -\frac{A}{2} + \frac{A}{t_r}t & 0 \leq t \leq t_r \\ \frac{A}{2} & t_r < t \leq t_r + t_H \\ \frac{A}{2} - \frac{A}{t_f}(t - t_r - t_H) & t_r + t_H < t \leq t_r + t_H + t_f \\ -\frac{A}{2} & t_r + t_H + t_f < t \leq T \end{cases} \tag{25}$$

Where A is the amplitude change. Thus, equation (24) can be re-expressed using (25). This can be smoothed using techniques such as spline interpolation or low-pass filtering, reducing the sharpness of the transitions, as follows:

$$tr_{smoothed}(t) = smooth(tr(t), method) \tag{26}$$

Where $smooth()$ refers to the smoothing function (e.g., LOESS or spline). The idea is that it creates a locally fitted polynomial for each section of the signal, producing smoother transitions, as expressed below:

$$tr_{smoothed}(t) = f_{LOESS}(t) \tag{27}$$

Where $f_{LOESS}(t)$ is a polynomial that fits the local data points, ensuring the slope of the signal changes more gradually than in the traditional trapezoidal case. This smoothing can be visualized as rounding the sharp corners of the traditional trapezoidal signal, making it easier for the converter to track the waveform and reducing stress on the power electronics components, as shown in Fig. 5.

It should be noted that the proposed smoothed trapezoidal may look similar to the sinusoidal signal with the third harmonic injection. But they are different. The smoothed trapezoidal signal demonstrates clear advantages in terms of compatibility with the NLC and reduced switching losses, thanks to its discrete nature and smoother transitions. Its lower THD compared to sinusoidal signals with the third harmonic injection ensures better power quality and reduced torque ripple in IM. Conversely, the sinusoidal signal excels in achieving a higher modulation index and lower intrinsic THD, making it ideal for scenarios prioritizing high efficiency and minimal EMI. However, its continuous nature and associated level quantization challenges make it less practical for discrete-level control in MMC systems. Overall, the proposed smoothed trapezoidal signal strikes a superior balance for MMC-based IM drives, combining practical implementation ease with improved harmonic performance.

A. SM Capacitor Voltage Balancing and Circulating Current Suppression

For an N-level PEBB concept with n SMs per arm, n SMs per leg are always ON to create $n + 1$ line-to-neutral voltages, meaning that the SM capacitor voltages must be selected according to the SM switching sequences. This paper balances the SM capacitor voltages in increasing or decreasing order, as shown in Fig. 4(a), depending on the direction of the arm current. For instance, in phase a of a five-level MMC, if one upper SM is ON (the other three upper SMs are OFF), three SMs of the lower arm are ON (the other lower SM is OFF). If two upper SMs are ON (the other two upper SMs are OFF), two SMs of the lower arm are ON (the other two lower SMs are OFF). With this modulation, the voltages across the capacitors in the converter are kept the same, leading to a completely symmetrical regime. This SM capacitor voltage balancing in the proposed NLC method is shown in Fig. 4(a) for the PEBB concept and how the staircase waveforms are shaped by switching SMs ON and OFF.

To suppress the circulating current while balancing the SM capacitor voltages, the direction of the arm current helps the decision-making strategy for the SM selection process. If the arm current is positive (greater than zero), the SMs with the lowest voltages are chosen in increasing order, and the rest of the SMs are bypassed. Similarly, if the arm current is negative (less than zero), the SMs with the highest voltages are chosen in decreasing order, and the rest of the SMs are bypassed. In other words, if the upper arm current is positive, it turns OFF the SMs with the highest voltages in the upper arm. Otherwise, it turns OFF the modules with the lowest voltage in the upper arm. The same procedure is applied to the lower arm current. This helps the circulating current suppression and SM capacitor voltage balancing simultaneously.

IV. Mathematical Model of Induction Machine

The electrical and electromechanical behavior of most synchronous machines can be understood using the equations for a three-phase salient-pole synchronous machine. This section establishes the voltage and electromagnetic torque equations in machine variables.

A. Voltage Equations in Machine Variables

The stator windings are identical and sinusoidally distributed, spaced 120° apart, with N_s equivalent turns and resistance r_s. Similarly, for this analysis, the rotor windings are also treated as three identical sinusoidally distributed windings, spaced 120° apart, with N_r equivalent turns and resistance r_r. The voltage equations in machine variables are given as follows [28]:

$$\mathrm{v}_{abcs} = \mathrm{r}_s \mathrm{i}_{abcs} + p\lambda_{abcs} \tag{28}$$

$$\mathrm{v}_{abcr} = \mathrm{r}_r \mathrm{i}_{abcr} + p\lambda_{abcr} \tag{29}$$

Where p represents the operator d/dt, the subscript s refers to variables and parameters associated with the stator circuits, and the subscript r refers to variables and parameters associated with the rotor circuits. Both r_s and r_r are diagonal matrices with identical, nonzero elements.

$$\mathrm{r}_s = \begin{bmatrix} r_{as} & 0 & 0 \\ 0 & r_{bs} & 0 \\ 0 & 0 & r_{cs} \end{bmatrix}, \mathrm{r}_r = \begin{bmatrix} r_{ar} & 0 & 0 \\ 0 & r_{br} & 0 \\ 0 & 0 & r_{cr} \end{bmatrix} \tag{30}$$

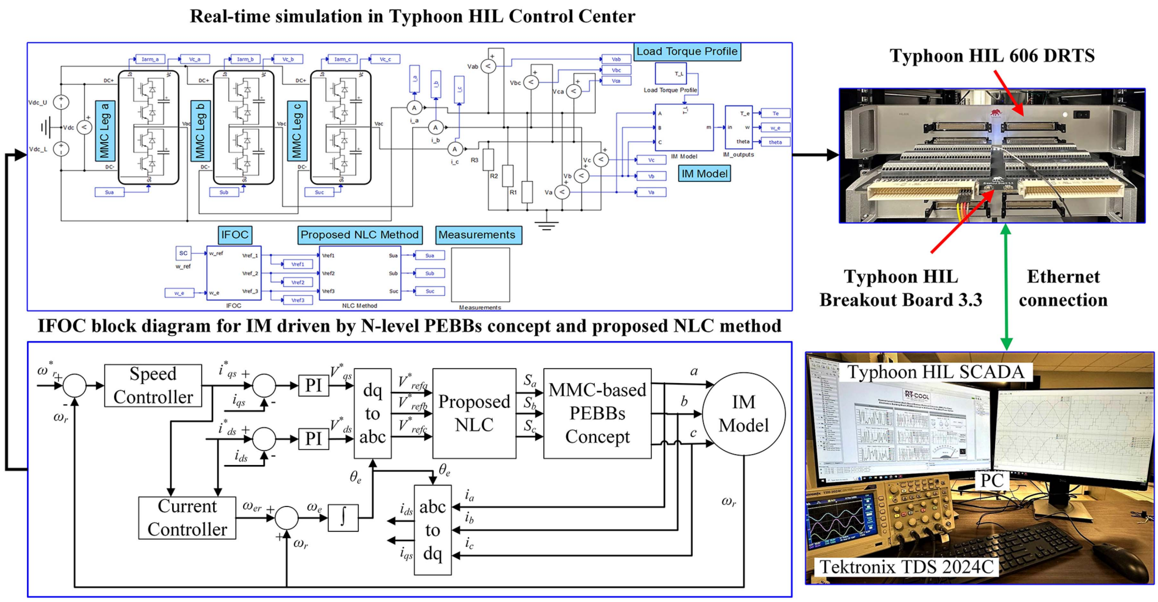

Fig. 6. Real-time setup simulation and IFOC block diagram for IM driven by N-level PEBBs concept in Typhoon HIL606 DRTS.

In a magnetically linear system, the flux linkages, as determined by the fundamental harmonic, can be represented as:

$$\begin{bmatrix}\lambda_{abcs}\\ \lambda_{abcr}\end{bmatrix} = \begin{bmatrix}\mathrm{L}_s & \mathrm{L}_{sr}\\ (\mathrm{L}_{sr})^T & \mathrm{L}_r\end{bmatrix}\begin{bmatrix}\mathrm{i}_{abcs}\\ \mathrm{i}_{abcr}\end{bmatrix} \tag{31}$$

Neglecting the mutual leakage between the stator and rotor windings, they can be represented as:

$$\mathrm{L}_s = \begin{bmatrix}L_{ls}+L_{ms} & -L_{ms}/2 & -L_{ms}/2\\ -L_{ms}/2 & L_{ls}+L_{ms} & -L_{ms}/2\\ -L_{ms}/2 & -L_{ms}/2 & L_{ls}+L_{ms}\end{bmatrix} \tag{32}$$

$$\mathrm{L}_r = \begin{bmatrix}L_{lr}+L_{mr} & -L_{mr}/2 & -L_{mr}/2\\ -L_{mr}/2 & L_{lr}+L_{mr} & -L_{mr}/2\\ -L_{mr}/2 & -L_{mr}/2 & L_{lr}+L_{mr}\end{bmatrix} \tag{33}$$

$$\mathrm{L}_{sr} = L_{sr}\begin{bmatrix}C(\theta_r) & C(\theta_r+\frac{2\pi}{3}) & C(\theta_r-\frac{2\pi}{3})\\ C(\theta_r-\frac{2\pi}{3}) & C(\theta_r) & C(\theta_r+\frac{2\pi}{3})\\ C(\theta_r+\frac{2\pi}{3}) & C(\theta_r-\frac{2\pi}{3}) & C(\theta_r)\end{bmatrix} \tag{34}$$

Where L_{ls} and L_{ms} denote the leakage and magnetizing inductances of the stator windings, respectively, while L_{lr} and L_{mr} refer to those of the rotor windings. The inductance L_{sr} represents the amplitude of the mutual inductance between the stator and rotor windings. And C stands for the cosine function. The referred rotor variables can be found in [28].

B. Torque Equation in Machine Variables

If P is the number of poles in the machine, so the motion equation is as follows:

$$\frac{\partial\omega_r}{\partial t} = \left(\frac{P}{2}\right)\frac{T_e - T_L}{J} \tag{35}$$

Where J represents the rotor's inertia, and T_L denotes the load torque, and the electrical torque is calculated with the following:

$$T_e = \left(\frac{P}{2}\right)(\mathrm{i}_{abcs})^T\frac{\partial}{\partial\theta_r}[\mathrm{L}_{sr}]\mathrm{i}_{abcr} \tag{36}$$

V. Real-Time Implementation Results

The MATLAB simulations of the proposed NLC were presented in [25] for a five-level PEBB. In that work, the NLC method was introduced using sinusoidal reference signals, and only a 5-level PEBB connected to an RL load was studied in MATLAB/Simulink. Here, the MATLAB simulation transitions into real-time implementation, introducing three significant extensions. First, smoothed trapezoidal reference signals are used to obtain improved output quality and control the modulation process. Second, the PEBB is connected to an IM, modeled in machine variables to capture the motor's dynamic behavior, featuring variable speed and torque loads. Third, the efficacy of the proposed NLC method expands to encompass N-level PEBBs to adjust voltage levels as required, broadening the scope and applicability of the study with Typhoon HIL606 DRTS. The real-time simulation is conducted for 9-level PEBBs, using parameters provided in Appendix A. Fig. 6 illustrates the real-time setup of the N-level PEBB and the IM within the Typhoon HIL606 DRTS. The model incorporates the DC-link, three PEBB legs, the proposed NLC method, the IM model, and the IFOC algorithm, with a block diagram also provided for illustration.

The proposed NLC method allows for the adjustment of the number of levels within the NLC block's component properties. The IFOC method is utilized for closed-loop IM speed and torque load control. This model is implemented in Typhoon HIL Control Center software to enable us to perform the real-time simulation which features a SCADA panel, as shown in Fig. 6,

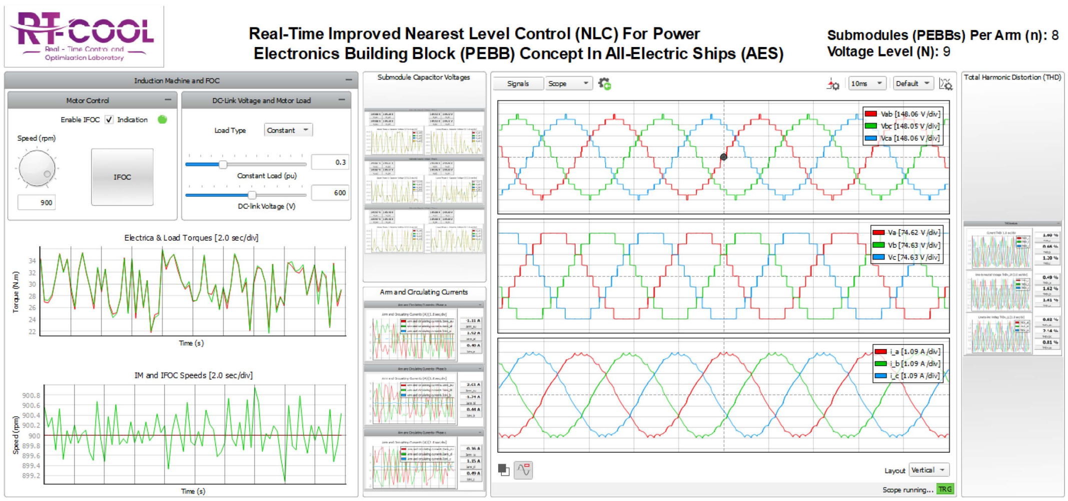

Fig. 7. Visualization dashboard and monitoring real-time results of the 9 L PEBB with proposed NLC method in Typhoon HIL SCADA.

providing users with a comprehensive view of the system's operation through various widgets and scopes. The simulation model, created in the Typhoon HIL Control Center, is compiled and loaded to the Typhoon HIL606 DRTS, which is connected to the Tektronix Digital Oscilloscope TDS2024 C through the Typhoon HIL Breakout Board 3.3 to monitor the results. The PC used for the simulation has 12th Gen Intel(R) Core(TM) i7-12700 2.10 GHz CPU and 16.0 GB RAM. In the following, the 9 L, 7 L, and 5 L PEBBs will be presented to assess the performance of the proposed NLC method for the PEBB concept with the IM model with machine variables. Lastly, the 9 L PEBB performance with variable speed and torque load, controlled by the IFOC method, will be analyzed.

A. Nine-Level PEBB Concept With IM

The results of a nine-level PEBB concept integrated with the IM model are outlined here. The results include simulation data from Typhoon HIL SCADA and real-time measurements obtained by Typhoon HIL606 DRTS using a Tektronix Digital Oscilloscope TDS2024 C. In the case of a nine-level (9 L) PEBB configuration, each arm comprises eight (8) SMs or PEBBs. The designed visualization dashboard and monitoring real-time results of 9 L PEBB are shown in Fig. 7. This figure presents several parts related to all different parts of the model including the parameters and settings related to IM such as IM and IFOC speeds, electrical and load torques, SM capacitor voltages, arm and circulating currents, input and output voltages and currents, and the THD analysis. This is further shown in Fig. 8. SM capacitor voltages of all phases are shown in Fig. 8(a), (c), and (e). As can be seen, the SM capacitor voltages are effectively balanced, hovering between 74.90 and 75.05 V. The arm and circulating currents are shown in Fig. 8(b), (d), and (f). They illustrate well-suppressed circulating currents, fluctuating around 330 to 520 mA. Finally, the line-to-line voltages, about 592.24 V, and phase currents which are nearly sinusoidal waveforms, about 4.36 A, are illustrated in Fig. 8(g) and (h), respectively.

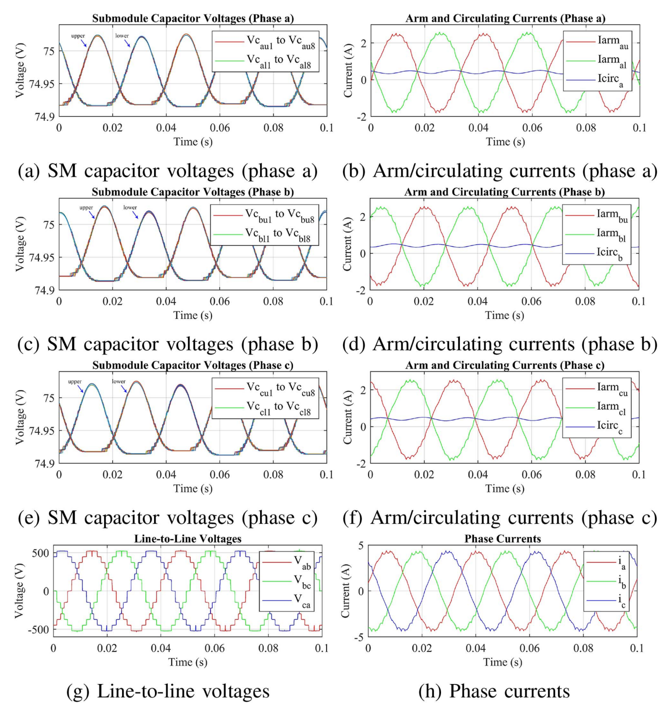

(a) SM capacitor voltages (phase a) (b) Arm/circulating currents (phase a)
(c) SM capacitor voltages (phase b) (d) Arm/circulating currents (phase b)
(e) SM capacitor voltages (phase c) (f) Arm/circulating currents (phase c)
(g) Line-to-line voltages (h) Phase currents

Fig. 8. Real-time results of the 9 L PEBB and proposed NLC method in Typhoon HIL SCADA.

Fig. 9 displays the real-time results (with Tektronix TDS2024 C) for the 9 L PEBB (phase a) while the IM speed is constant at 900 rpm and torque load is constant at 30 N.m. Fig. 9(a) illustrates SM capacitor voltages (SM No.: 2, 7, 13, 16) at about 75 V. Arm voltages are maintained at about 600 V (Fig. 9(b)). Arm and circulating currents remain steady at about 2.4A and 340 mA, respectively (Fig. 9(c)). Finally, Fig. 9(d) shows the DC-link voltage of nearly 600 V, the line-to-neutral voltage of about 298.52 V, the line-to-line voltage of almost 596.8 V, and the current of approximately 4.4A.

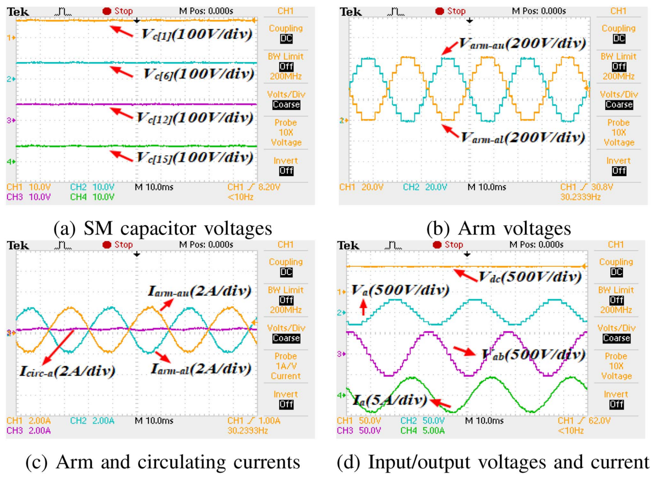

(a) SM capacitor voltages (b) Arm voltages (c) Arm and circulating currents (d) Input/output voltages and current

Fig. 9. Real-time results of the 9 L PEBB and proposed NLC method in TDS2024 C oscilloscope.

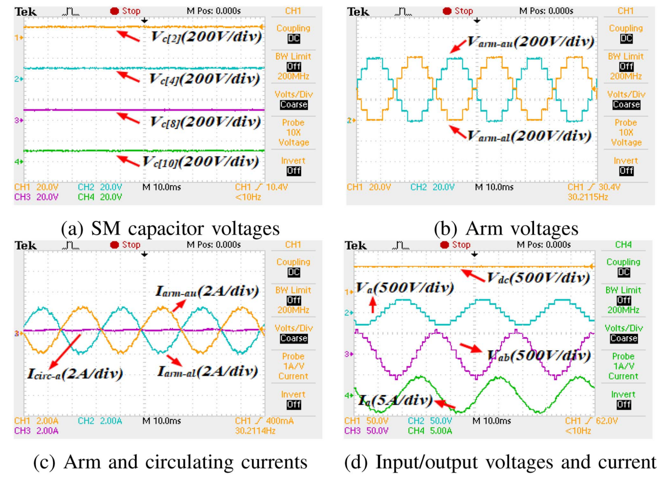

(a) SM capacitor voltages (b) Arm voltages (c) Arm and circulating currents (d) Input/output voltages and current

Fig. 11. Real-time results of the 7 L PEBB and proposed NLC method in TDS2024 C oscilloscope.

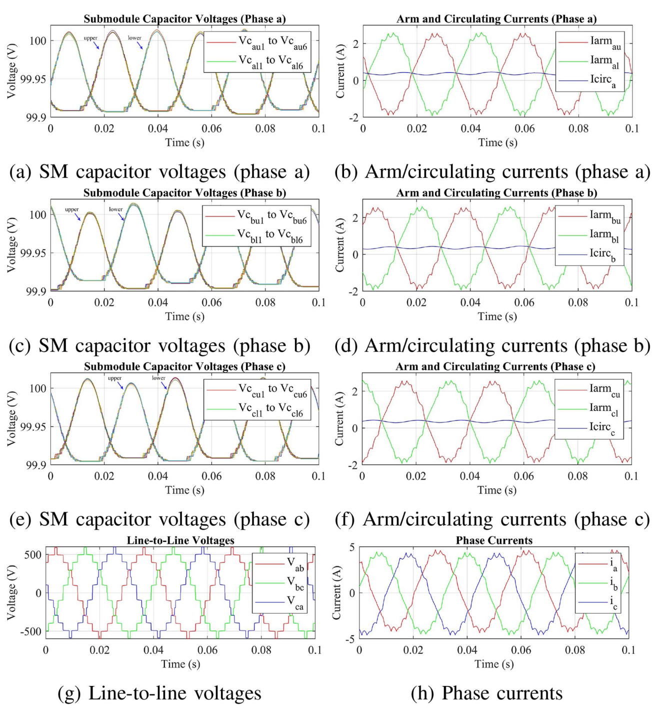

(a) SM capacitor voltages (phase a) (b) Arm/circulating currents (phase a) (c) SM capacitor voltages (phase b) (d) Arm/circulating currents (phase b) (e) SM capacitor voltages (phase c) (f) Arm/circulating currents (phase c) (g) Line-to-line voltages (h) Phase currents

Fig. 10. Real-time results of the 7 L PEBB and proposed NLC method in Typhoon HIL SCADA.

B. Seven-Level PEBB Concept With IM

The results of a seven-level PEBB concept integrated with the IM model are outlined here. The results include simulation data from Typhoon HIL SCADA and real-time measurements obtained by Typhoon HIL606 DRTS using a Tektronix Digital Oscilloscope TDS2024 C. In the case of a seven-level (7 L) PEBB configuration, each arm comprises six (6) SMs or PEBBs. SM capacitor voltages of all phases are shown in Fig. 10(a), (c), and (e). As can be seen, the SM capacitor voltages are effectively balanced, hovering between 99.89 V and 100.00 V. The arm and circulating currents are shown in Fig. 10(b), (d), and (f). They illustrate well-suppressed circulating currents, fluctuating around 400 to 510 mA. Finally, the line-to-line voltages, about 592.24 V, and phase currents which are nearly sinusoidal waveforms, about 4.36 A, are illustrated in Fig. 10(g) and (h), respectively.

Fig. 11 displays the real-time results (with Tektronix TDS2024 C) for the 7 L PEBB (phase a) while the IM speed is constant at 900 rpm and torque load is constant at 30 N.m. Fig. 11(a) illustrates SM capacitor voltages (SM No.: 3, 5, 9, 11) at about 100 V. Arm voltages are maintained at about 600 V (Fig. 11(b)). Arm and circulating currents remain steady at about 2.3A and 390 mA, respectively (Fig. 11(c)). Finally, Fig. 11(d) shows the DC-link voltage of nearly 600 V, the line-to-neutral voltage of about 295.32 V, the line-to-line voltage of almost 590.4 V, and the current of about 4.82A.

C. Five-Level PEBB Concept With IM

The results of a five-level PEBB concept integrated with the IM model are outlined here. In the case of a five-level (5 L) PEBB configuration, each arm comprises four (4) SMs or PEBBs. SM capacitor voltages of all phases are shown in Fig. 12(a), (c), and (e). As can be seen, the SM capacitor voltages are effectively balanced, hovering between 149.87 V and 149.98 V. The arm and circulating currents are shown in Fig. 12(b), (d), and (f). They illustrate well-suppressed circulating currents, fluctuating around 400 to 490 mA. Finally, the line-to-line voltages, about 592.24 V, and phase currents which are nearly sinusoidal waveforms, about 5 A, are illustrated in Fig. 12(g) and (h), respectively.

Fig. 13 displays the real-time results (with Tektronix TDS2024 C) for the 5 L PEBB (phase a) while the IM speed is constant at 900 rpm and torque load is constant at 30 N.m. SM capacitor voltages (SM No.:1, 4, 5, 8) remain stable at about 150 V (Fig. 13(a)). Arm voltages are maintained at about 600 V (Fig. 13(b)). Arm and circulating currents remain steady at about 3 A and 500 mA, respectively (Fig. 13(c)). Finally, as shown in Fig. 13(d), the current is about 4.95 A while the DC-link, line-to-neutral and line-to-line voltages are about 600 V, 293.56 V, and 593.2 V, respectively.

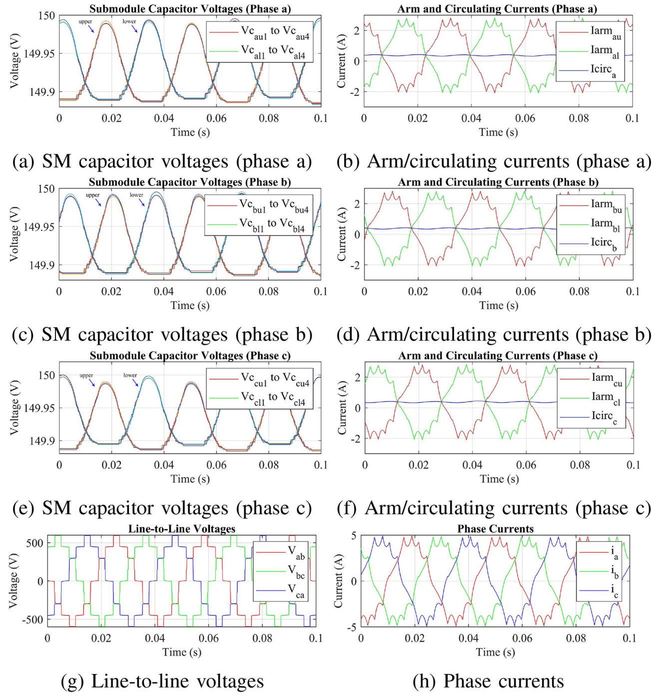

(a) SM capacitor voltages (phase a) (b) Arm/circulating currents (phase a)

(c) SM capacitor voltages (phase b) (d) Arm/circulating currents (phase b)

(e) SM capacitor voltages (phase c) (f) Arm/circulating currents (phase c)

(g) Line-to-line voltages (h) Phase currents

Fig. 12. Real-time results of the 5 L PEBB and proposed NLC method in Typhoon HIL SCADA.

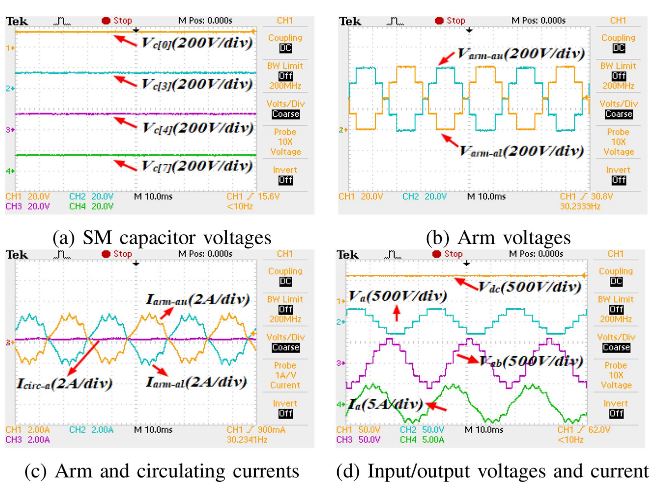

(a) SM capacitor voltages (b) Arm voltages

(c) Arm and circulating currents (d) Input/output voltages and current

Fig. 13. Real-time results of the 5 L PEBB and proposed NLC method in TDS2024 C oscilloscope.

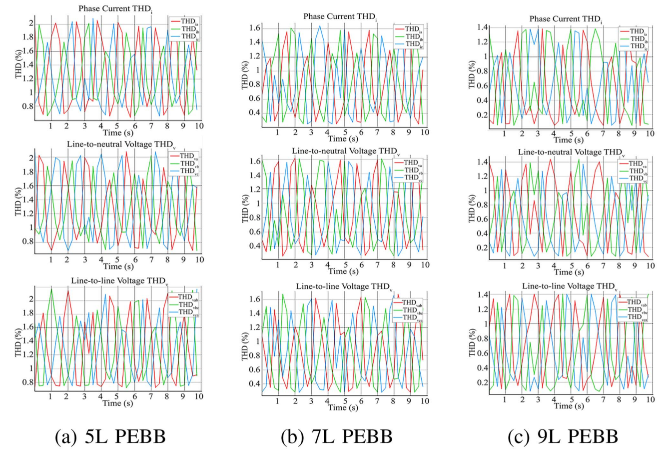

(a) 5L PEBB (b) 7L PEBB (c) 9L PEBB

Fig. 14. Real-time THD analysis of the different levels of PEBBs and proposed NLC method in Typhoon HIL SCADA. Sampling time is 250 ms, and from top to bottom: THDs of phase currents, line-to-neutral voltages, and line-to-line voltages.

D. THD Analysis and Comparison

Fig. 14(a) to (c) illustrate the THD analysis of all discussed five-level, seven-level, and nine-level PEBBs, respectively. The subfigures, from top to bottom, are the THD of currents, line-to-neutral voltages, and line-to-line voltages, respectively, which are well within the standard limits.

Table III presents a comparative analysis of various NLC approaches for MMCs, including the improved NLC method proposed in this work. The table evaluates each approach based on the number of SMs per arm, circulating current controllability, current THD, voltage THD, and complexity. The conventional NLC method, while simple to implement, exhibits relatively poor output quality. Level-increased NLC approaches, while improving output quality, often lack effective circulating current control or robust SM capacitor voltage ripple management. Recent advancements, such as Modified NLC, additional-level-based control with model predictive control (ALC-MPC), and nearest vector control (NVC), have incorporated mechanisms to control circulating currents. However, these methods may introduce additional complexity or potentially compromise output quality. The proposed improved NLC method offers a compelling solution by achieving a significant enhancement in output quality while maintaining a relatively low level of complexity. This approach is adaptable to a wide range of SM counts (N-level, 5 L/7L/9 L presented in this paper) and effectively addresses the challenges of circulating current control and output waveform distortion.

TABLE III
COMPARISON OF DIFFERENT NLC APPROACHES

Approach	Year	SM Per Arm	Circ. Current Control	Current THD	Voltage THD	Complexity
Conventional NLC [18]	2011	20	No	High	High	Low
Level-increased NLC [22]	2015	10	No	Avg.	Avg.	Low
Predictive NLC [29]	2015	8,50	Good	Low	High	High
Level-increased NLC [24]	2016	8	Limited	Low	Low	Medium
NLC-C [30]	2016	20	Limited	Low	Low	Medium
Modified NLC [31]	2017	10	Good	Low	High	Medium
Level-increased NLC [32]	2020	10	Good	Low	Low	High
Modified NLC [16]	2020	7	Good	Low	Low	Medium
ALC-MPC [33]	2023	20	Good	Low	Low	High
NVC [34]	2024	16	Good	Low	Low	Medium
Proposed improved NLC	–	4,6,8	Good	Low	Low	Low

E. PEBB With Variable Speed and Torque Load

In order to evaluate the performance of the system further, the load profile of an actual AES is applied in this section. In our previous works [35], [36], we introduced the zonal ship power

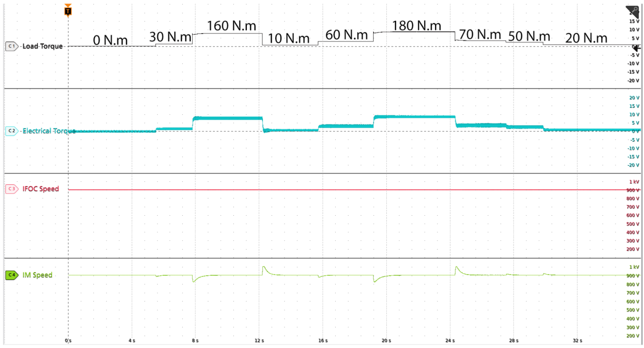

(a) Variable load torque and constant speed

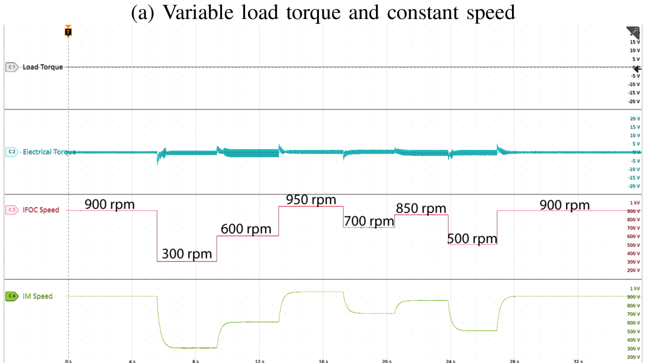

(b) Variable speed and constant load torque

Fig. 15. Real-time results of PEBB under different torque loads and speeds (sampling time is 250 ms) with MSO58 oscilloscope.

system, which was proposed for use in US Navy AESs. In this system, various zones and parts have distinct load profiles, with the Propulsion Motor Module (PMM) being the most critical. In this case, the PMM comprises two propulsion units, making it the primary focus in AESs. The PMM load profile was taken for around 3500 seconds. Here, in this paper, the 9 L PEBBs are considered for analysis of varying the load torque and speed. The full load profile of the PMM for 12000 seconds is scaled down and applied to the IM model used in the system.

Fig. 15(a) displays the implemented load torque profile, the electrical load, the IFOC reference speed, and the IM speed in Tektronix 5 series Mixes Signal Oscilloscope MSO58. The load torque starts at 0 N.m, then steps up to 30 N.m, while the speed briefly downward speed spikes to 895 rpm before stabilizing at 900 rpm. Then, the load torque dramatically increases to 160 N.m when the speed drops to 850 rpm before returning to 900 rpm. When the torque load drops to 10 N.m, opposite upward speed spikes occur, in this case, up to around 1000 rpm before coming back to 900 rpm. As can be seen for the rest of the torque and speed waveform, depending on how much the load torque changes, the electrical torque and speed change follow the same pattern.

For further evaluation, the system's performance is analyzed under varying speed conditions while maintaining a constant load torque, which is set to zero in this case. Fig. 15(b) illustrates the load and electrical torques, the applied IFOC reference speed pattern, and the IM speed. Initially, the speed is 900 rpm, and the torque remains unchanged, with a steady error of 5 N.m. When the speed abruptly drops to 300 rpm, the torque temporarily spikes to approximately -28 N.m before stabilizing. Subsequently, as the speed increases to 600 rpm and then to 950 rpm, the torque spikes to about 10 N.m and 15 N.m, respectively, before returning to its initial value. This behavior is consistently observed during subsequent speed variations.

VI. Conclusion

This paper proposes an enhanced N-level NLC method, utilizing smoothed trapezoidal reference signals instead of sinusoidal ones to improve the performance of PEBBs in AESs. The proposed NLC method offers a versatile solution for adjusting voltage levels as needed while simultaneously enhancing power quality, capacitor voltage balancing, and circulating current suppression. The smoothed trapezoidal reference signals in the proposed N-level NLC method provide better output voltage quality and control the modulation process. The real-time implementation's validation on an IM model with machine variables, representative of real-world AESs, including variations in speed and torque loads, is presented. Through comprehensive analysis of Typhoon HIL606 DRTS across 9 L/7L/5 L PEBB setups, the real-time results demonstrate the superior efficacy of the NLC switching method, highlighting its real-time adaptability and effectiveness. It enhances power output quality, reduces voltage and current quantization, optimizes the balancing of capacitor voltages in the SMs, and more effectively suppresses circulating currents. Furthermore, this work extends to diverse operating conditions, including variations in torque loads and speeds controlled via the IFOC method, reaffirming the robustness and adaptability of the PEBB system with the proposed NLC switching method.

For future work, the fault ride-through capability of the proposed NLC in the PEBB for AESs deserves consideration to validate its performance further under unhealthy conditions. Optimized SM sorting considering switching losses as a higher number of SMs results in higher power losses. Similarly, voltage stress ratios can be analyzed.

Appendix

PEBB parameters are DC-link voltage $V_{dc} = 600\,\text{V}$, number of PEBBs per arm $n = 4, 6, 8$, SM capacitance $C_m = 5\,\text{mF}$, arm inductance $L_{arm} = 5\,\text{mH}$, arm resistance $R_{arm} = 0.25\,\Omega$, switching frequency $F_{sw} = 10\,\text{kHz}$, execution rate $T_s = 100\,\mu\text{s}$, and simulation step time $1\,\mu\text{s}$. IM parameters are stator phase resistance $r_s = 13.12\,\Omega$, rotor phase resistance referred to the stator $r_r = 11.202\,\Omega$, stator leakage inductance $L_{ls} = 0.0276\,\text{H}$, rotor leakage inductance referred to the stator $L_{lr} = 0.0194\,\text{H}$, magnetizing inductance $L_M = 0.3482\,\text{H}$, number of pole pairs is 2, combined rotor and load moment of inertia $J = 0.015\,\text{kg}\cdot\text{m}^2$, and no machine viscous friction coefficient. IFOC current and speed controllers' parameters are $k_i = 34.35$, $k_p = 0.046$, $k_{iw} = 60.81$, and $k_{pw} = 10.52$.

Acknowledgment

The authors would like to acknowledge the Warren H. Owen Distinguished Professorship Endowment for its support of the research effort.

References

[1] G. Sulligoi, A. Vicenzutti, and R. Menis, "All-electric ship design: From electrical propulsion to integrated electrical and electronic power systems," *IEEE Trans. Transp. Electrific.*, vol. 2, no. 4, pp. 507–521, Dec. 2016.

[2] T. Ericsen, N. Hingorani, and Y. Khersonsky, "Power electronics and future marine electrical systems," *IEEE Trans. Ind. Appl.*, vol. 42, no. 1, pp. 155–163, Jan./Feb. 2006.

[3] N. H. Doerry and D. H. Clayton, "Shipboard electrical power quality of service," in *Proc. 2005 IEEE Electric Ship Technol. Symp.*, 2005, pp. 274–279.

[4] S. I. Rahman et al., "Emerging trends and challenges in thermal management of power electronic converters: A state of the art review," *IEEE Access*, vol. 12, pp. 50633–50672, 2024.

[5] A. Moghassemi, S. M. I. Rahman, G. Ozkan, C. S. Edrington, Z. Zheyu, and P. K. Chamarthi, "Power converters coolant: Past, present, future, and a path toward active thermal control in electrified ship power systems," *IEEE Access*, vol. 11, pp. 91620–91659, 2023.

[6] S. Choudhury, M. Bajaj, T. Dash, S. Kamel, and F. Jurado, "Multilevel inverter: A survey on classical and advanced topologies, control schemes, applications to power system and future prospects," *Energies*, vol. 14, no. 18, 2021, Art. no. 5773.

[7] P. Qashqai, A. Sheikholeslami, H. Vahedi, and K. Al-Haddad, "A review on multilevel converter topologies for electric transportation applications," in *Proc. 2015 IEEE Veh. Power Propulsion Conf.*, 2015, pp. 1–6.

[8] H. Mahdi, B. Hoff, and T. Østrem, "A review of power converters for ships electrification," *IEEE Trans. Power Electron.*, vol. 38, no. 4, pp. 4680–4697, Apr. 2023.

[9] D. Ronanki, S. A. Singh, and S. S. Williamson, "Comprehensive topological overview of rolling stock architectures and recent trends in electric railway traction systems," *IEEE Trans. Transp. Electrific.*, vol. 3, no. 3, pp. 724–738, Sep. 2017.

[10] Q. Xu et al., "Analysis and comparison of modular railway power conditioner for high-speed railway traction system," *IEEE Trans. Power Electron.*, vol. 32, no. 8, pp. 6031–6048, Aug. 2017.

[11] M. Vasiladiotis and A. Rufer, "Analysis and control of modular multilevel converters with integrated battery energy storage," *IEEE Trans. Power Electron.*, vol. 30, no. 1, pp. 163–175, Jan. 2015.

[12] L. Timilsina et al., "Degradation abatement in hybrid electric vehicles using data-driven technique," *Transp. Res. Procedia*, vol. 70, pp. 52–60, 2023.

[13] L. Timilsina et al., "A real-time prognostic-based control framework for hybrid electric vehicles," *IEEE Access*, vol. 11, pp. 127589–127607, 2023.

[14] Y. Chen, Z. Li, S. Zhao, X. Wei, and Y. Kang, "Design and implementation of a modular multilevel converter with hierarchical redundancy ability for electric ship mvdc system," *IEEE J. Emerg. Sel. Topics Power Electron.*, vol. 5, no. 1, pp. 189–202, Mar. 2017.

[15] H. Song et al., "A compact high-power single-turn inductor for 6 kV SiC-based power electronics building blocks," in *Proc. IEEE 22nd Workshop Control Modelling Power Electron.*, 2021, pp. 1–8.

[16] M. H. Nguyen and S. Kwak, "Nearest-level control method with improved output quality for modular multilevel converters," *IEEE Access*, vol. 8, pp. 110237–110250, 2020.

[17] S. Kouro, R. Bernal, H. Miranda, C. A. Silva, and J. Rodríguez, "High-performance torque and flux control for multilevel inverter fed induction motors," *IEEE Trans. Power Electron.*, vol. 22, no. 6, pp. 2116–2123, Nov. 2007.

[18] Q. Tu and Z. Xu, "Impact of sampling frequency on harmonic distortion for modular multilevel converter," *IEEE Trans. Power Del.*, vol. 26, no. 1, pp. 298–306, Jan. 2011.

[19] W. Wang, K. Ma, and X. Cai, "Flexible nearest level modulation for modular multilevel converter," *IEEE Trans. Power Electron.*, vol. 36, no. 12, pp. 13686–13696, Dec. 2021.

[20] Z. Li, P. Wang, H. Zhu, Z. Chu, and Y. Li, "An improved pulse width modulation method for chopper-cell-based modular multilevel converters," *IEEE Trans. Power Electron.*, vol. 27, no. 8, pp. 3472–3481, Aug. 2012.

[21] G. Si, J. Zhu, Y. Lei, L. Jia, and Y. Zhang, "An enhanced level-increased nearest level modulation for modular multilevel converter," *Int. Trans. Elect. Energy Syst.*, vol. 29, no. 1, 2019, Art. no. e2669.

[22] P. Hu and D. Jiang, "A level-increased nearest level modulation method for modular multilevel converters," *IEEE Trans. Power Electron.*, vol. 30, no. 4, pp. 1836–1842, Apr. 2015.

[23] D. Anupom, D.-C. Shin, and D.-M. Lee, "Scheme for reducing harmonics in output voltage of modular multilevel converters with offset voltage injection," *J. Power Electron.*, vol. 19, no. 6, pp. 1496–1504, 2019.

[24] L. Lin, Y. Lin, Z. He, Y. Chen, J. Hu, and W. Li, "Improved nearest-level modulation for a modular multilevel converter with a lower submodule number," *IEEE Trans. Power Electron.*, vol. 31, no. 8, pp. 5369–5377, Aug. 2016.

[25] A. Moghassemi et al., "Nearest level control based modular multi-level converters for power electronics building blocks concept in electric ship system," in *Proc. 2024 IEEE Transp. Electrific. Conf. Expo*, 2024, pp. 1–6.

[26] P. J. Sotorrio-Ruiz, F. J. Sanchez-Pacheco, F. M. Perez-Hidalgo, and J. R. Heredia-Larrubia, "Modulation of a trapezoidal signal: Improving signal quality and reducing costs in power inverters," *IET Power Electron.*, vol. 10, no. 5, pp. 568–576, 2017.

[27] M. Kurtoğlu and A. M. Vural, "A novel nearest level modulation method with increased output voltage quality for modular multilevel converter topology," *Int. Trans. Elect. Energy Syst.*, vol. 2022, no. 1, 2022, Art. no. 2169357.

[28] P. C. Krause, O. Wasynczuk, S. D. Sudhoff, and S. Pekarek, *Analysis of Electric Machinery and Drive Systems*. Piscataway, NJ, USA: IEEE Press/Wiley Interscience, 2002.

[29] F. Zhang and G. Joos, "A predictive nearest level control of modular multilevel converter," in *Proc. 2015 IEEE Appl. Power Electron. Conf. Expo.*, 2015, pp. 2846–2851.

[30] D. Wu and L. Peng, "Characteristics of nearest level modulation method with circulating current control for modular multilevel converter," *IET Power Electron.*, vol. 9, no. 2, pp. 155–164, 2016.

[31] X. Chen, J. Liu, S. Ouyang, S. Song, and H. Wu, "A modified circulating current suppressing strategy for nearest level control based modular multilevel converter," in *Proc. IEEE Energy Convers. Congr. Expo.*, 2017, pp. 1817–1822.

[32] X. Chen, J. Liu, S. Song, and S. Ouyang, "Circulating harmonic currents suppression of level-increased NLM based modular multilevel converter with deadbeat control," *IEEE Trans. Power Electron.*, vol. 35, no. 11, pp. 11418–11429, Nov. 2020.

[33] Q. Yu, F. Deng, Y. Tang, Y. Wang, and F. Blaabjerg, "Additional-levels-based control method for modular multilevel converters with reduced dc-link current ripple," *Int. J. Elect. Power Energy Syst.*, vol. 153, 2023, Art. no. 109288.

[34] Y. N. Bakir, S. de Pablo, F. Martinez-Rodrigo, Z. A. Aljawary, and L. C. Herrero-de Lucas, "Nearest vector control method applied to an MMC for PV generation," *Energies*, vol. 17, no. 8, 2024, Art. no. 1795.

[35] C. S. Edrington et al., "Distributed energy management for ship power systems with distributed energy storage," *J. Mar. Eng. Technol.*, vol. 19, no. 1, pp. 31–44, 2020.

[36] T. V. Vu et al., "Large-scale distributed control for MVDC ship power systems," in *Proc. IECON 44th Annu. Conf. IEEE Ind. Electron. Soc.*, 2018, pp. 3431–3436.

Ali Moghassemi (Graduate Student Member, IEEE) received the B.S. and M.S. degrees in electrical engineering from Islamic Azad University, South Tehran Branch, Tehran, Iran, in 2012 and 2015, respectively. He is currently working toward the Ph.D. degree with Real-Time COntrol and Optimization Laboratory (RT-COOL), Holcombe Department of Electrical and Computer Engineering, Clemson University, Clemson, SC, USA. He is also a Graduate Research Assistant of electrical engineering with Real-Time Control and Optimization Laboratory (RT-COOL), Holcombe Department of Electrical and Computer Engineering, Clemson University, under the supervision of Dr. Christopher S. Edrington. He has authored and coauthored several peer-reviewed papers in high-quality journals and conferences, two book chapters, and one book. His research interests include electro-thermal modeling, simulation, and control of power electronics building blocks (PEBBs) in all-electric ships (AESs). He is also a volunteer reviewer for several peer-reviewed journals/conferences over the years.

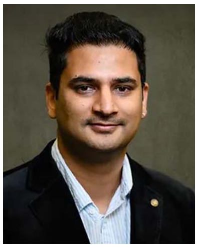

Laxman Timilsina (Member, IEEE) received the B.E. degree in electrical engineering from the Institute of Engineering, Tribhuvan University, Dharan, Nepal, in 2016, the M.Sc. degree in distributed generation in electrical engineering from the Institute of Engineering, in 2019, and the Ph.D. degree in electrical engineering from Clemson University, Clemson, SC, USA, in May 2024, under the mentorship of Dr. Christopher S. Edrington. In Fall 2021, he enrolled with Clemson University, to work toward the Ph.D. degree. He was a Graduate Research Assistant with the Real-Time COntrol and Optimization Laboratory (RT-COOL), The Holcombe Department of Electrical and Computer Engineering, Clemson University, where he is currently a Postdoctoral Researcher Fellow. His research interests include electrified vehicles, integration of renewable energy, ship power systems, and smartgrids.

S M Imrat Rahman (Graduate Student Member, IEEE) received the B.Sc. degree in electrical and electronic engineering from the Islamic University of Technology, Gazipur City, Bangladesh, in 2010, and the M.Sc. degree in power engineering from the Technical University of Munich, Munich, Germany, in 2015. He is currently working toward the Ph.D. degree with the Holcombe Department of Electrical and Computer Engineering (ECE), Clemson University, Clemson, SC, USA, under the supervision of Dr. Christopher S. Edrington and Dr. Gokhan Ozkan. He is also a Graduate Research Assistant with the Real-Time COntrol and Optimization Laboratory (RT-COOL), Holcombe Department of ECE, Clemson University. His research interests include active thermal management of power electronic converters, distributed control, and thermal modeling of power electronic building blocks (PEBB) systems.

Ali Arsalan (Graduate Student Member, IEEE) received the bachelor's degree in electronics engineering from the University College of Engineering & Technology, Islamia University of Bahawalpur, Bahawalpur, Pakistan, in 2015, and the master's degree in electrical engineering from the University of Engineering and Technology, Lahore, Pakistan, in 2019. He is currently working the Ph.D. degree in automotive engineering with Clemson University, SC, USA. From January 2017 to August 2022, he was a Laboratory Engineer with the Khwaja Fareed University of Engineering and Information Technology (KFUEIT), Pakistan. He is also a Graduate Research Assistant with the Secure Energy and Automation Laboratory (SEAL), International Center for Automotive Research (ICAR), Greenville, SC, USA. His research interests include optimization, microgrids, energy management, EV technologies, cyber security, and power system resiliency toward cyber threats.

Grace Muriithi received the B.Sc. degree in electrical engineering from the Jomo Kenyatta University of Agriculture and Technology, Juja, Kenya, and the M.Sc. degree in electrical engineering from the University of Cape Town, Cape Town, South Africa. She is currently working toward the Ph.D. degree in automotive engineering with the International Centre for Automotive Research, Clemson University, Clemson, SC, USA. She is also undertaking research in resilience and security enhancement of cyber-physical systems, with a particular focus on (hybrid) electric vehicles (HEVs) and electric vehicle charging stations (EVCSs). Her research interests include cyber-physical systems security, machine learning, energy management, microgrids, and vulnerability analysis in advanced control systems.

Elutunji Buraimoh (Member, IEEE) received the Bachelor of Technology (B.Tech.) degree (with Hons.) in electronic and electrical engineering from the Ladoke Akintola University of Technology, Ogbomosho, Nigeria, in 2012, the Master of Science (M.Sc.) degree in electronic and electrical engineering from Obafemi Awolowo University, Osun, Nigeria, in 2016, and the Doctor of Engineering (Ph.D.) degree in electrical engineering from the Durban University of Technology, Durban, South Africa. His research interests include inverter-based microgrids, renewable energy, power systems control, and FACTS devices.

Gokhan Ozkan (Senior Member, IEEE) received the B.S. degree in teacher training from Marmara University, Istanbul, Türkiye, in 2006, the B.S. degree in electrical field and energy system engineering, and the M.S. degree in energy system engineering from Erciyes University, Kayseri, Türkiye, in 2014 and 2016, respectively, and the Ph.D. degree in electrical and computer engineering from the FAMU-FSU College of Engineering, Tallahassee, FL, USA. He was a Lecturer with Bozok University, Yozgat Merkez/Yozgat, Türkiye. He was a Graduate Research Assistant with the Center for Advanced Power Systems, Florida State University, Tallahassee. He is currently a Research Assistant Professor with the Real-Time COntrol and Optimization Laboratory (RT-COOL), Clemson University, Clemson, SC, USA. His research interests include renewable energy real-time modeling, simulation, control design, and electro-thermal management for power converters.

Behnaz Papari (Senior Member, IEEE) received the Ph.D. degree in electrical engineering from Florida State University, Tallahassee, FL, USA, in 2018. She was an Assistant Professor in power electronics engineering and the Manager with Duke Energy Smart Grid Laboratory. She was also Associated with the Energy Production and Infrastructure Center (EPIC), University of North Carolina at Charlotte, Charlotte, NC, USA. She is currently with the Department of Marine Engineering Technology, Texas A&M University at Galveston, Galveston, TX, USA. She has expertise in power systems with an emphasis on modeling, analysis, control, planning, and optimization. Her specialties are distributed controls and decision analysis under uncertainty, applications on energy system modeling, and stochastic optimization. Her research interests include renewable energy sources, power and energy management, control of stand-alone and utility-interactive energy systems, distributed control of smart grids, stochastic analysis, real-time power distribution system simulation, and hardware-in-the-loop instantiation.

Christopher S. Edrington (Senior Member, IEEE) received the B.S. degree in engineering from Arkansas State University, Jonesboro, AR, USA, in 1999, and the M.S. and Ph.D. degrees in electrical engineering from the Missouri University of Science and Technology, Rolla, MO, USA, in 2001 and 2004, respectively. He was a DoE GAANN Fellow, NSF IGERT Fellow, and Grainger Foundation Fellow with the Missouri University of Science and Technology. He is currently the Warren H. Owen Distinguished Professor of electrical and computer engineering with Clemson University, Clemson, SC, USA. He is also the Lead with Real-Time COntrol and Optimization Laboratory (RT-COOL) and the Co-Director of the Smart Energy and Propulsion Focus Area in the new VIrtual PRototyping for Ground vehicle Systems (VIPR-GS) Center. He has authored or coauthored more than 170 papers, including two IEEE Prize awards and multiple conference paper awards. He has graduated 23 M.S. Students and 16 Ph.D. Students (with three in process). He has also six patents (in real-time stability and complexity metrics). His research interests include modeling, simulation, and control of electromechanical drive systems, applied power electronics, distributed control, integration of renewable energy, storage, and pulse power loads.

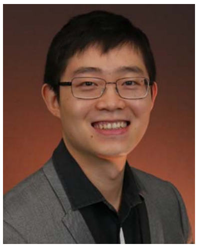

Zheyu Zhang (Senior Member, IEEE) received the B.S. and M.S. degrees in electrical engineering from the Huazhong University of Science and Technology, Wuhan, China, in 2008 and 2011, respectively, and the Ph.D. degree in electrical engineering from The University of Tennessee, Knoxville, TN, USA, in 2015. From 2015 to 2018, he was a Research Assistant Professor with the Department of Electrical Engineering and Computer Science, University of Tennessee, Knoxville, TN, USA, Lead Power Electronics Engineer of general electric research with Niskayuna, NY, USA, from 2018 to 2019, and Warren H. Owen' Duke Energy Assistant Professor of Engineering with Clemson University, Clemson, SC, USA, from 2019 to 2023. He is currently an Assistant Professor with Rensselaer Polytechnic Institute, Troy, NY, USA. He has authored or coauthored more than 100 papers in the most prestigious journals and conference proceedings, filed more than ten patent applications, has authored one book and one book chapter, and presented more than ten IEEE tutorial seminars and webinars. His research interests include wide bandgap-based power electronics characterization and applications. Dr. Zhang was the recipient of four prize Paper awards from the IEEE Industry Applications Society (IAS) and IEEE Power Electronics Society, 2021 IEEE IAS Andrew W. Smith Outstanding Young Member Achievement Award, and 2022 NASA Early Career Faculty Award. He is currently an Associate Editor for IEEE Transactions on Power Electronics and IEEE Transactions on Industry Applications. He is also the Standard Vice-Chair of IEEE IAS Power Electronics Devices and Components Committee.

Phani Kumar Chamarthi (Member, IEEE) received the joint M.Tech. and Ph.D. degrees from the Department of Electrical and Electronics Engineering, Indian Institute of Technology Bombay, Mumbai, India, in 2018, with a specialization in power electronics and power systems. Between 2022 and 2023, he was a Postdoctoral Fellow with Clemson University, Clemson, SC, USA. His research interests include new single-stage transformerless inverter topologies, multilevel converter topologies, space vector control of multilevel converters, and new modulation and control strategies of multilevel converters with a focus on renewable energy applications.